RESEARCH ARTICLE

Key Points:
- Good agreement between simulated and observed nonorographic gravity waves
- Intrinsic frequencies of the order of 5–10 times the inertial frequency
- Moist convection and strong stratospheric winds contribute to the waves

Correspondence to:
R. Plougonven,
riwal.plougonven@polytechnique.org

Case studies of nonorographic gravity waves over the Southern Ocean emphasize the role of moisture

Riwal Plougonven[1], Albert Hertzog[1], and M. Joan Alexander[2]

[1]Laboratoire de Météorologie Dynamique, IPSL, Ecole Polytechnique, Palaiseau, France, [2]NWRA/Colorado Research Associates, Boulder, Colorado, USA

Abstract Two case studies of nonorographic gravity waves are carried out for wave events that occurred over the Southern Ocean in November 2005. Mesoscale simulations were carried out with the Weather and Research Forecast model. The simulated waves were compared to observations from superpressure balloons of the Vorcore campaign and from the High Resolution Dynamic Limb Sounder satellite. Satisfactory agreement is found, giving confidence in the estimations of wave parameters and amplitudes. For the amplitudes, both the model and observations provide a lower bound, for different reasons. Waves are found in the lower stratosphere with horizontal wavelengths of the order of 150–200 km in the horizontal, 5–8 km in the vertical, corresponding to intrinsic frequencies between 5 and 10 f, where f is the Coriolis parameter. Although the tropospheric flow is very different between the two cases, there are features which are common and appear significant for the gravity waves: these include intense localized updrafts associated with convection in the troposphere and a displaced polar vortex inducing strong winds in the stratosphere above the frontal region. Relative to theoretical expectations, the simulations emphasize the role of moisture. Intrinsic frequencies are significantly higher than those expected for waves produced by dry spontaneous generation from jets. To quantify the contribution of moisture, dry simulations were carried out, yielding momentum fluxes over oceanic regions that were 2.5 times weaker. Identification of the generation mechanisms in these complex flows calls for further study, and these should include moisture and a realistic stratospheric jet.

1. Introduction

Internal gravity waves matter, among other reasons, for the global circulation of the atmosphere because of the momentum fluxes that result from their propagation upward into the stratosphere and mesosphere. The forcing of the mean circulation that results from their dissipation is responsible for essential features of the middle atmosphere's temperature and wind distributions [*Fritts and Alexander*, 2003]. Because of their relatively short scales (typically from 10 to ~1000 km), most of these waves are usually represented in climate models by parameterizations [*Kim et al.*, 2003]. These parameterizations have been and remain an important source of uncertainty for climate simulations that include a stratosphere (e.g., *Austin et al.* [2003]; *Butchart et al.* [2010]).

One of the main challenges in improving current parameterizations of atmospheric gravity waves concerns the description of the *sources of nonorographic waves*. Whereas orographic gravity waves have been modeled for decades [*Queney*, 1948], sources of nonorographic gravity waves are only beginning to be explicitly described (i.e., explicitly related to the modeled flow) in parameterizations. Models of convectively generated waves have been developed and have served as a basis for parameterizations over the last decade [*Beres et al.*, 2004, 2005; *Song and Chun*, 2005]. This mainly concerns the tropics, where convection is the dominant source of waves. In contrast, jets and fronts in midlatitudes have only seldom been parameterized explicitly, with only qualitative justifications for the diagnostic used as a source (shear in *Rind et al.* [1988] and frontogenesis function in *Charron and Manzini* [2002] and *Richter et al.* [2010]). Yet there exists multiple observational evidence of their importance: for example, satellite observations show that the gravity wave activity is strongly enhanced during winter over the jet/storm track region, even more than in the tropics and subtropics [*Yan et al.*, 2010; *Ern et al.*, 2011]. Further evidence comes from the analysis of the contributions to momentum fluxes over the Southern Ocean and the Antarctic Peninsula: although the
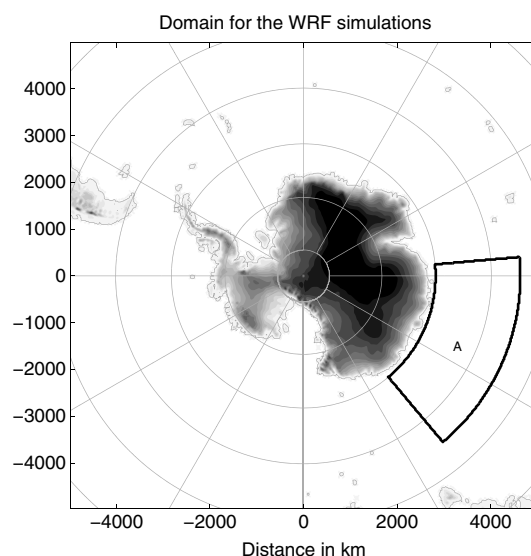
Figure 1. Domain of the numerical simulations and limits of region *A* (thick black line) used to identify episodes of intense momentum fluxes due to gravity waves appropriate for investigation. Latitude shown every 10° starting from 85°S and longitude shown every 30°. Horizontal coordinates are *x* and *y* axes, values are in kilometers. Grey shading shows the height of the topography, contour interval of 250 m.

orographic waves yield a conspicuous local maximum, the integrated fluxes from nonorographic waves are comparable [*Hertzog et al.*, 2008; *Plougonven et al.*, 2013].

Observations have shown that jet/front systems are important sources of waves for midlatitudes [*Fritts and Nastrom*, 1992; *Eckermann and Vincent*, 1993]. One flow configuration that has been very much emphasized as favorable to the presence of intense gravity waves is jet exit regions [*Uccelini and Koch*, 1987; *Guest et al.*, 2000; *Pavelin et al.*, 2001; *Plougonven et al.*, 2003]. Gravity waves have often been found with low intrinsic frequencies, propagating both upward and downward away from the jet [*Yamanaka et al.*, 1989; *Thomas et al.*, *Sato and Yoshiki*, 1999; 2008], though waves have also been found emitted from surface fronts [*Ralph et al.*, 1999].

A difficulty for the theoretical modeling of gravity waves originating from jets and fronts comes from the complexity of the flow in which they are generated: near-surface or upper level fronts, in regions and at times where the flow is fully three dimensional and time dependent [*Plougonven and Zhang*, 2014]. Now the dynamics of midlatitude jet/front systems has mainly been understood, theoretically, using balanced models [e.g., *Hoskins et al.*, 1985], the simplest and most widely used being the quasi-geostrophic approximation [cf. *Vallis*, 2006, and references therein]. Frontogenesis requires a higher-order balanced approximation, and semigeostrophy was elaborated for this purpose [*Hoskins and Bretherton*, 1972; *Hoskins*, 1982]. Yet this remains a balanced model and hence excludes gravity waves by construction. It is necessary to go beyond these balanced approximations in order to describe the emission of gravity waves. Classical asymptotic approaches, for flows with small Rossby number, do not describe the emission of gravity waves from balanced flows [*Reznik et al.*, 2001; *Zeitlin*, 2008]. The coupling of balanced motions and gravity waves can be calculated analytically in constant shear flows [*Vanneste*, 2004; *Plougonven et al.*, 2005; *Lott et al.*, 2010, 2012] and is found to be exponentially weak in Rossby number [*Vanneste*, 2008, 2013].

Theoretical investigations of spontaneous emission have used idealized numerical simulations to go beyond the simple flow configurations that can be considered analytically. Simulations of baroclinic life cycles have produced internal gravity waves which had common features with waves observed in the vicinity of jets and fronts: low-frequency waves were found in jet exit regions, where the flow is diffluent and strong deformation of the horizontal wind is present [*O'Sullivan and Dunkerton*, 1995; *Zhang*, 2004; *Plougonven and Snyder*, 2005, 2007]. These simulations used dry dynamics only, yet the flow generating the waves retained significant complexity as it is fully three dimensional and time evolving.

Understanding of the generation of these Jet Exit Region Emitted (JEREmi) waves has been provided by simplifying the flow further to focus on dipoles. A dipole constitutes a simple model of an upper level jet streak [*Cunningham and Keyser*, 2000]. Simulations of dipoles in a stratified, rotating fluid have been conducted by different groups, with very different models [*Snyder et al.*, 2007; *Viudez*, 2007, 2008; *Wang et al.*, 2009], and a robust phenomenology has emerged: low-frequency waves with phase lines transverse to the flow are found in the exit region, with characteristics consistent with those favored by propagation in the background shear and strain. The waves are explained as perturbations linearized on the background of the dipole flow, forced by the small discrepancy between balanced and full tendencies [*Snyder et al.*, 2009; *Wang et al.*, 2010; *Wang and Zhang*, 2010].

The understanding of JEREmi waves constitutes a significant advance, and it is necessary to investigate how the emitted waves change when the baroclinic life cycles become more realistic (e.g., include moist
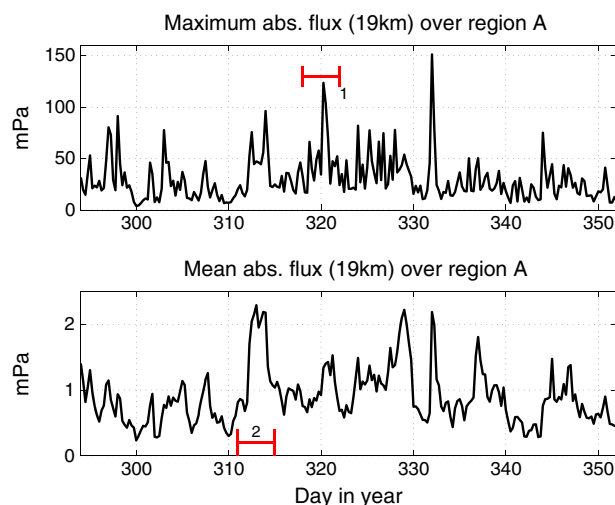
Figure 2. Time series of the (top) maximum and (bottom) mean of the gravity wave momentum fluxes over region *A*, at altitude $z = 19$ km from 21 October, 00:00 UT, to 18 December, 00:00 UT. Horizontal axis is in days in year 2005, and vertical axis is in millipascal. The periods for case studies 1 and 2 are indicated by red bars.

processes). One route for this consists in including moisture in idealized baroclinic life cycles. Studies along this path indicate more intense emission [*Waite and Snyder*, 2012; *Wei and Zhang*, 2014; *Mirzaei et al.*, 2014]. However, conclusions from such studies will always include uncertainties due to the fact that the source itself includes processes that are parameterized (convection) and sensitivity to the initial distribution of humidity that is imposed. Another route consists in examining case studies for which observations provide a reliable counterpart to check the simulation results. A disadvantage is that each case study is by essence specific, and a large number of cases would be needed to attempt to generalize the conclusions. An advantage is that observations of these gravity waves provide a good assessment of the realism of the model simulations.

A unique data set describing stratospheric gravity waves comes from long-duration superpressure balloons [*Hertzog and Vial*, 2001], from which momentum fluxes can be derived [*Vincent et al.*, 2007; *Boccara et al.*, 2008]. These fluxes are "*considered the most accurate global-scale measurements available, for waves with intrinsic frequencies $\hat{\omega}$ lower than $2\pi (1 \text{ h})^{-1}$*" [*Geller et al.*, 2013]. The Vorcore campaign (September 2005 to February 2006) consisted in 27 balloons launched in the Southern Hemisphere's polar vortex from McMurdo in Antarctica [*Hertzog et al.*, 2007]. Analysis of the momentum fluxes showed that, although the strongest values found are clearly tied to orographic waves above the Antarctic Peninsula "hot spot," fluxes due to nonorographic waves contributed at a level at least comparable to orographic waves when integrated over all the oceanic regions [*Hertzog et al.*, 2008]. Another source of global observations of gravity waves comes from the HIRDLS (High Resolution Dynamic Limb Sounder) instrument aboard the Aura satellite [*Gille et al.*, 2008]. Its horizontal and vertical resolutions make it a significant source of information on gravity waves [*Alexander et al.*, 2008]. Comparisons of the estimations of gravity waves from the balloon and satellite measurements have been carried out, using Probability Distribution Functions (PDFs) and have proved very encouraging [*Hertzog et al.*, 2012]. This comparison also included a PDF of momentum fluxes obtained from mesoscale simulations, which also compared well with the balloon estimations. These mesoscale simulations are described by *Plougonven et al.* [2013] (PHG hereafter), with a more detailed comparison of the simulated gravity waves and the observations from the Vorcore balloons. The average fluxes agreed well over the ocean (underestimation by a factor ∼0.8 in the simulations), i.e., for nonorographic sources. Detailed comparison for individual wave events lays outside the scope of this previous study and constitutes the major purpose of the present one.

The aims of the present study are thus to pursue, via case studies, the comparisons between gravity waves simulated in a mesoscale model and available observations (superpressure balloons and satellite) and to take advantage of the mesoscale simulations to explore flow features leading to significant generation of gravity waves. Our focus is on nonorographic gravity waves only. The present study continues and complements PHG and hence uses the same set of mesoscale simulations. The present work is part of a more general effort to bring together available sources of information on gravity waves to quantify them, their associated fluxes, and resulting forcing of the middle atmosphere more accurately [*Alexander et al.*, 2010; *Geller et al.*, 2013]. This aims at contributing to the improvement of gravity wave parameterizations in climate models.

The paper is organized as follows: the simulations and observations used are described in section 2. The two case studies are described in sections 3 and 4, respectively. The interpretation and implications of the results are discussed in section 5, before concluding remarks in section 6.
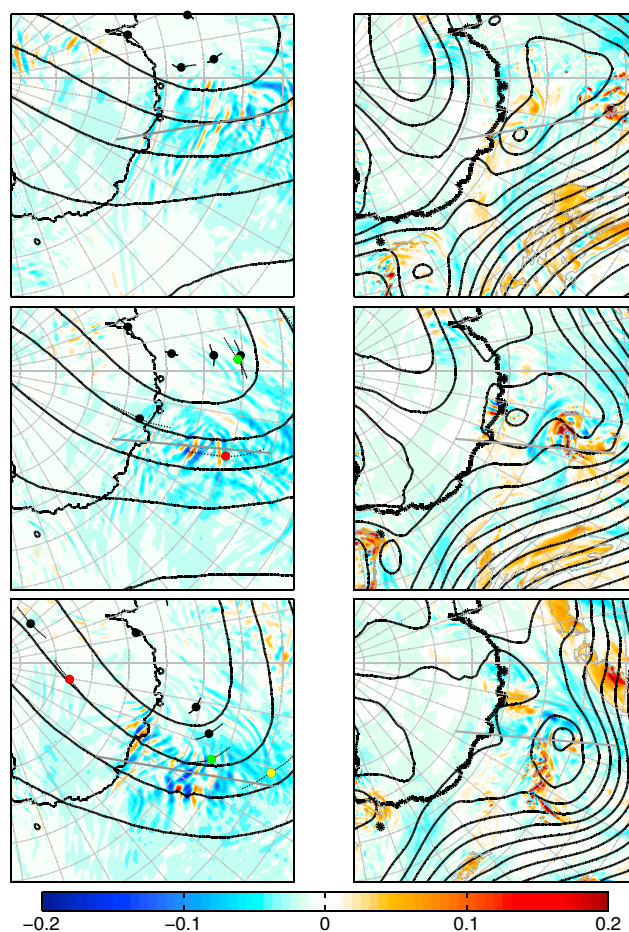
Figure 3. Maps of the vertical velocity (colors, in m s^{-1}) at (left) $z = 20$ km and (right) $z = 5$ km, for times (top) 319.0, (middle) 319.75, and (bottom) 320.5. Also shown are isobars (contour intervals 2 hPa (left) and 4 hPa (right), and the location of the vertical cross sections presented in Figure 4 (thick gray lines). The positions of the balloons available are shown on the maps at $z = 20$ km (left). The large dots indicate the location at the time of the snapshot of vertical velocity, with colors used to identify three balloons discussed in the text: #3 (red), #8 (green), and #22 (yellow). The smaller, black dots indicate the balloon locations during the 3 h prior and posterior to the snapshot. Also shown on the maps at $z = 5$ km (right) is one contour for the ice content at that altitude, corresponding to 0.06 g of ice per kilogram of air (thin gray line).

2. Model Setup and Data

2.1. Mesoscale Model Simulations

The simulations were run with the Weather Research and Forecast Model (WRF) [*Skamarock et al.*, 2008] and have been described in PHG. The domain is 10,000 km × 10,000 km (see Figure 1) and extends in the vertical to 5 hPa (about 36 km). The horizontal resolution is $\Delta x = 20$ km, and 120 levels are used in the vertical. A sponge layer is active in the upper 5 km of the model domain, with a damping affecting only vertical motions in order to damp gravity waves and avoid their reflection from the model top. Choices of parameterizations for moist processes follow that advised for cold regions, following work on National Center for Atmospheric Research's Antarctic Mesoscale Prediction System [*Wang et al.*, 2012]: the microphysics is handled by the WRF single-moment five-class scheme, and the cumulus parameterization is the Kain-Fritsch scheme. Analyses from the European Centre for Medium-Range Weather Forecasts (ECMWF) were used for the initialization and for the boundary conditions. The simulations are free running (there is no nudging toward the analysis in the interior of the domain) and were hence limited to 3 days as a compromise between the necessary spin-up (24 h; see *Plougonven et al.* [2010]) and predictability of the flow. Simulations were started every 3 days from 20 October 2005, 00:00 UT, to 15 December 2005, 00:00 UT, a period for which numerous balloon observations from the Vorcore campaign were available over the ocean. Hence, the period for which simulations can be used spans 58 days, from 21 October, 00:00 UT,
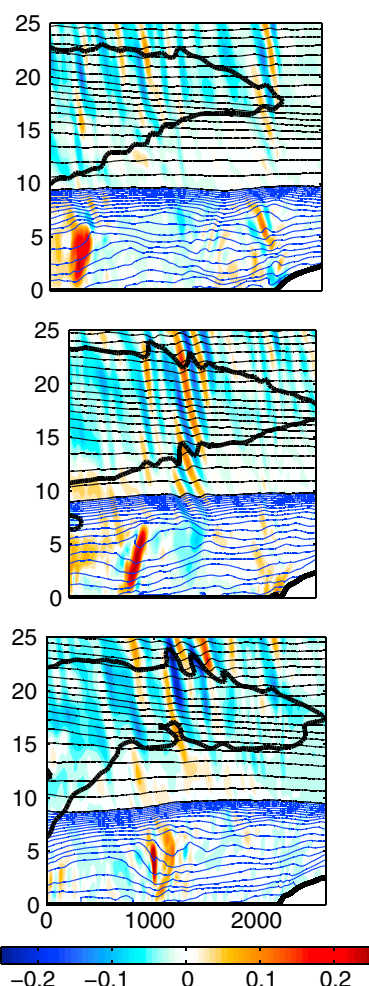
Figure 4. Vertical cross sections of the vertical velocity (colors, in m s^{-1}) for days (top) 319.0, (middle) 319.75, and (bottom) 320.50 at the locations shown in Figure 3 (left). Also shown are isentropes (blue lines with contour interval 2.5 K up to 320 K and black lines with contour interval 20 K above that) and the isotach for $|\mathbf{u}| = 35$ m s^{-1} (thick black line). The x axis shows the horizontal coordinate, and y axis shows the vertical coordinate, with values in kilometer.

to 18 December, 00:00 UT, with model outputs stored every 6 h. Below, time will often be referred to using the day in year (e.g., 21 October, 00:00 UT, corresponds to day 294.0).

PHG compared the overall gravity wavefield between the simulations and the balloon observations. Over the ocean, the average fluxes were found to be comparable, with an average underestimation in the simulations by a factor 0.8 relative to the observations. Detailed investigation of significant events was left for further study, and this is the purpose of the present paper. The focus being on pursuing the comparison and investigation of these existing simulations, only a limited number of new, dedicated simulations, has been carried out.

2.2. Balloon Observations

As mentioned in section 1, the balloon data set used in this study has been gathered during the 27 flights of superpressure balloons performed in the frame of the 2005 Vorcore campaign in Antarctica [*Hertzog et al.*, 2007]. Balloons drifting around 17 km (75 hPa) and 19 km (55 hPa) for more than 2 months on average were used during this campaign. The balloons were launched within the stratospheric polar vortex in late winter/early spring, and most of them drifted close to the vortex edge until the vortex breakdown in mid-December.

Details on the onboard instruments and measurement can be found in *Hertzog et al.* [2007]. Briefly, the vertical fluxes of zonal, meridional, and absolute horizontal gravity wave momentum are estimated from the observations by computing the correlation between horizontal- and vertical-velocity disturbances induced by gravity waves [*Hertzog and Vial*, 2001; *Boccara et al.*, 2008]. While the horizontal-velocity disturbances are directly measured, the vertical ones are deduced from the vertical displacement of the isopycnal surface on which the balloons are flying. Due to the 15 min sampling period of Vorcore observations, only waves with intrinsic periods longer than 1 h are considered in this data set.

2.3. Satellite Observations

Temperature profiles retrieved from HIRDLS measurements are analyzed for gravity waves. HIRDLS is an infrared limb sounder with rapid vertical scanning and coverage from cloud tops to the mesosphere in 15–16 s [*Gille et al.*, 2008]. The rapid scan rate gives a close separation between profiles along the measurement track of ~100 km. In addition, the line of sight lies at a 47° angle from the orbital plane, so the field of view projected on the limb defines the resolution of the measurements. This resolution is 10 km × 1.2 km along track and ~150 km along the line of sight. *Gille et al.* [2008] give an overview of the measurements and temperature retrieval. Measurements in the Southern Hemisphere are limited to latitudes north of 65°S, but at these high southern latitudes the HIRDLS 100 km horizontal sampling is advantageous for resolution of zonally propagating gravity waves. Retrieval noise was estimated at ~0.5 K or less in the lower stratosphere.

The analysis method used in our study to extract information on gravity waves examines temperature profiles along 3000 km segments of HIRDLS measurements crossing through an area of interest during a gravity wave event in early November 2005. Gravity waves are analyzed as deviations from a parabolic fit to the horizontal temperature variations along the measurement track. This may remove some larger-scale gravity waves, but in practice it is found that the scale separation between the waves of interest and other temperature variations is sufficient so that the wave signal is not sensitive to the specific choice made for the filtering (see section 4.2). The resulting small-scale temperature variations will be compared
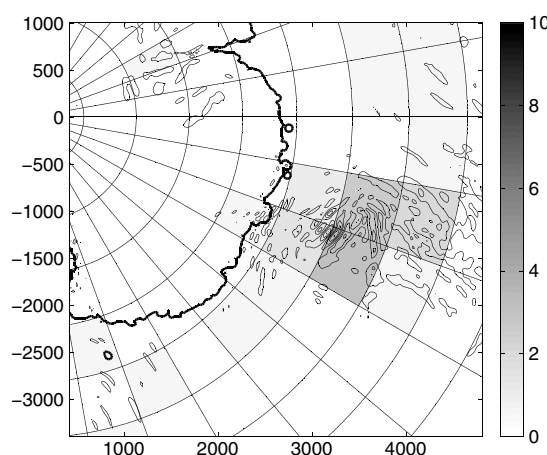
Figure 5. Simulated momentum fluxes on day 319.75, at 20 km altitude, averaged in boxes 10° longitude by 5° latitude. Gray scale is shown on the right, in millipascal. Also shown, as a reminder of the location of the wave packets, are contours of vertical velocity at the same level, every 0.05 m s^{-1}. Horizontal coordinates are shown in kilometer.

to model output sampled along the HIRDLS measurement track at the closest model output time to the measurement.

2.4. Choice of Case Studies

The purpose of the present case studies being to study cases of nonorographic gravity waves, a region over the ocean has been delimited, far from islands and far from the coastline. This region (region *A*) is shown in Figure 1, and its location should guarantee that waves found in the lower stratosphere are of nonorographic origin.

Momentum fluxes at an altitude of 20 km are used as a criterion to identify gravity wave episodes most worthwhile to investigate. The choice of the altitude is guided by the comparison to the balloons but does not affect the results significantly (cf. PHG on vertical variations of the gravity wavefield in the lower stratosphere).

Figure 2 shows the maximum and mean momentum fluxes from the WRF simulations found over region *A* during the 2 months of simulations. Note that the maximum values are calculated from the model output at each grid point, i.e., they are not averaged in space or time. First we note that there is moderate intermittency, even averaged over this fairly broad area, as has been emphasized in previous studies [*Alexander et al.*, 2010; *Hertzog et al.*, 2012; *Plougonven et al.*, 2013]. Second, we identify a certain number of peaks during the period corresponding to episodes of intense gravity wave activity. Other criteria included the availability of appropriate observations, the timing in the season, with a preference for earlier dates and for events that occur far enough from lateral boundaries. Two episodes were selected, one corresponding to a large value for the local maximum (120 mPa, episode 1; see section 3) and the other corresponding to a large value for the mean momentum fluxes in this time series (episode 2; see section 4). Two other episodes appear as interesting candidates, on days 328 and 332. The waves in the latter case, however, appear too close to the lateral boundary.

3. Case Study 1: Days 319 and 320

In the present section we describe the first case study, corresponding to the large values of maximum local momentum fluxes, found for days 319–320, i.e., 15–16 November 2005. We first describe the gravity waves as they appear in the simulations (section 3.1). The available observations are used to assess the realism of the simulations (section 3.2). The simulations are then used to describe the underlying tropospheric flow (section 3.3) and discuss possible generation mechanisms (section 3.4).

3.1. Modeled Gravity Waves

The wave event is described by two simulations, one started on day 317.00 and the next started on day 319.00. At the time corresponding to the transition from one simulation to the next (i.e., day 320.00, after the 24 h spin-up of the second simulation), it is found that the stratospheric gravity waves in the two simulations share many similarities (location, orientation, amplitude, and wavelengths) but of course differ in their details (see Appendix A). Below we discuss general characteristics of the wave event and no longer refer to the two different simulations.

The gravity waves present in region *A* display a clear, conspicuous region of enhanced wave activity during day 319 (15 November 2005) and the beginning of day 320 (16 November). This is illustrated in Figure 3 (left) by maps of the vertical velocity at altitude $z = 20$ km, taken at 18 h interval, from day 319 to day 320.50. From the start, a region of enhanced gravity waves is present. It shifts during the day, eastward and somewhat poleward at a velocity of about 15 m s^{-1}. Maximum anomalies of vertical wind reach 0.2 m s^{-1}. The extent of this region is roughly 1000 km in the meridional direction and 600 km in the zonal direction.
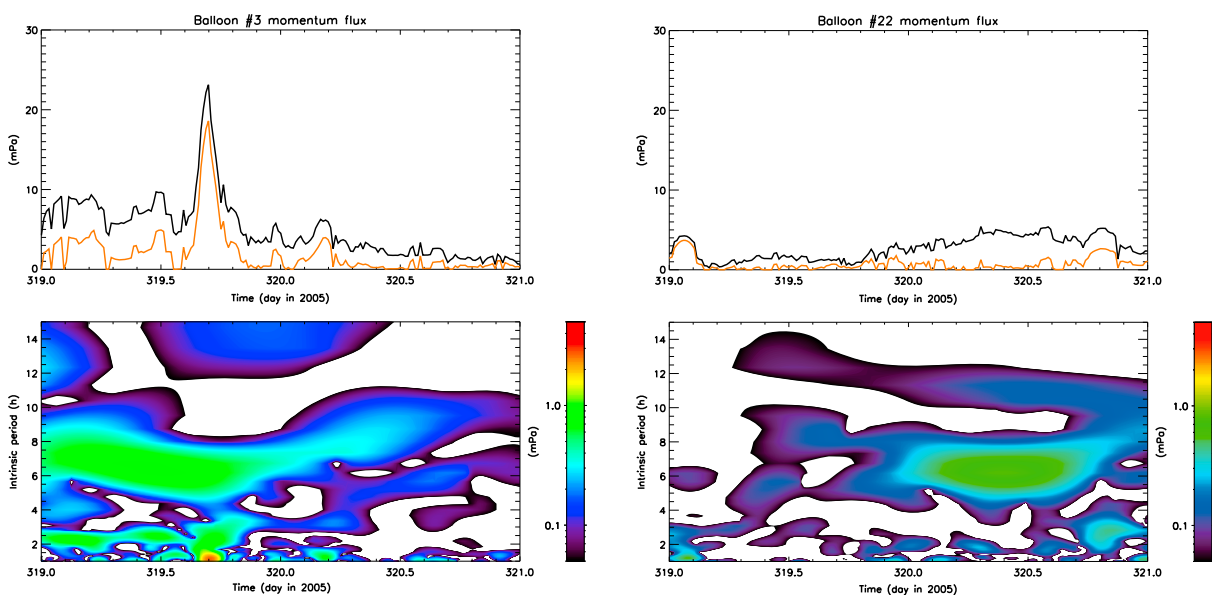
Figure 6. Analysis of momentum fluxes for balloons (left) #3 and (right) #22. (top) Time series of gravity wave absolute momentum fluxes in millipascal. Whereas the black curve shows the total flux, the red curve shows the contribution from waves with intrinsic periods shorter than 3 h. (bottom) Wavelet decomposition of the momentum flux time series above, showing at each time (horizontal axis) the contribution from waves with different intrinsic periods (vertical axis). The color scale gives the spectral amplitude of the wavelet analysis.

Whereas the signal on day 319.00 appears somewhat disorganized, the structure of two wave packets becomes clear from day 319.50 onward. Maps at lower stratospheric levels (e.g., 15 km) show similar signals (not shown).

The vertical structure of the waves is illustrated in Figure 4 using vertical cross sections of the vertical velocity. An extended region of the flow in the lower stratosphere contains significant oscillations of vertical velocity (amplitudes greater than 0.1 m s^{-1}). Conspicuous wave packets come out in several places, with stronger intensities and well-defined wavelengths (e.g., around $s = 1200$ km for day 319.75, where s is the horizontal distance along the section). Identification of the wavelengths and other characteristics at an altitude of 20 km is made from such plots and confirmed using individual profiles (not shown). Wavelengths are 150–180 km in the horizontal and 7–9 km in the vertical, yielding an intrinsic frequency of $9.6 \pm 2\,f$.

A key quantity for the impact on the middle atmosphere will be momentum fluxes. These can be estimated from the wave characteristics or by direct calculation from the simulations. We focus on the absolute momentum fluxes, i.e., $\overline{\rho u'_{\parallel} w'}$, with $u'_{\parallel}$ the velocity in the direction of the wave vector [Hertzog et al., 2008]. These fluxes can be estimated by two different calculations, which provide a check on the consistency of the description of the waves:

1. Using the characteristics given above ($150 < \lambda_h < 180$ km, $7 < \lambda_z < 9$ km), a typical amplitude of $\hat{w} \sim 0.1$–0.15 m s^{-1}, polarization relations from linear theory [e.g., Fritts and Alexander, 2003] and values of buoyancy frequency calculated from the simulation (about 0.02 s^{-1}) one finds values for the local momentum fluxes typically around 25–30 mPa.
2. From the simulations, the small-scale part of the velocity field (scales less than 1000 km) is isolated using a moving window average. Zonal and meridional momentum fluxes are then calculated at each grid point as $\rho u' w'$ and $\rho v' w'$. The absolute momentum flux is obtained as $\rho \sqrt{(u' w')^2 + (v' w')^2}$ (see PHG for further details). These calculations yield local maxima typically between 30 and 45 mPa, consistent with the above estimation.

When calculating momentum fluxes, it is important to specify the scales on which the fluxes are calculated. When averaged in boxes 10° longitude by 5° latitude, as was done in PHG for comparison with estimations from the balloons [Hertzog et al., 2008], absolute momentum fluxes calculated from the simulations yield maximum values of the order of 3.2 mPa on day 319.75, as illustrated in Figure 5. It increases further to reach 6.8 mPa on day 320.5 and then decays down to 2.2 mPa by day 321.00.
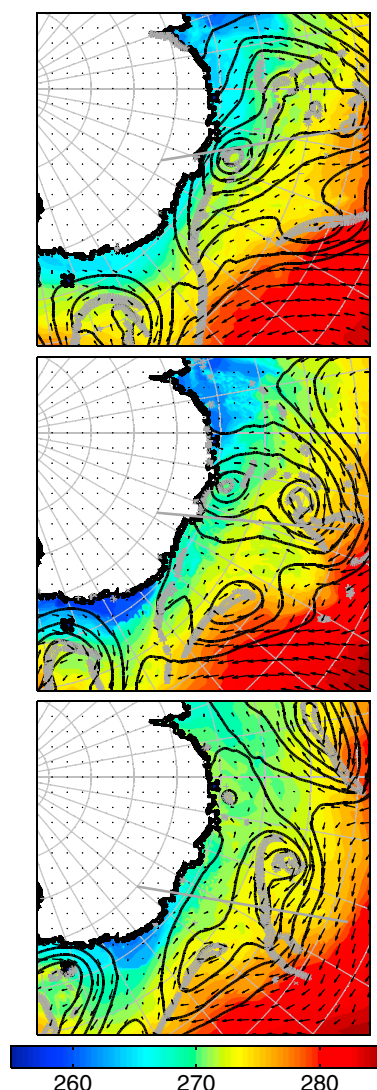
Figure 7. Surface flow for days (top) 319.0, (middle) 319.75, and (bottom) 320.50, described by the distribution of the surface temperature (colors, in Kelvin), surface pressure (thick black lines, contour interval: 4 hPa), 10 m wind (black arrows), and the relative vorticity of the surface winds (thick gray line, one contour for value $0.25\,f$, where f is the local value of the Coriolis parameter).

3.2. Observed Gravity Waves

In the present section we turn to observations to assess the realism of the simulated waves. Balloon trajectories are depicted in Figure 3, showing for instance that Vorcore balloon #3 was flying through the main wave packet simulated at day 319.75.

Figure 6 (left) shows the time series of the momentum flux estimated from measurements of balloon #3. A clear, localized peak is found at day 319.70, reaching absolute momentum flux of 23.1 mPa. This flux is mainly due to the contribution (18.6 mPa) from waves with short intrinsic periods (<3 h) and the wavelet decomposition of the signal clearly shows that this event is due to a wave packet with relatively short intrinsic period, of the order of an hour (1.09 h, corresponding to a frequency of 12.7 f, where f is the Coriolis parameter). The time resolution of the observations unfortunately does not allow a good description of such waves (one measurement point every 15 min), and hence, this wave event is likely underestimated in these balloon observations. Nonetheless, we retain a remarkable agreement between the balloon estimate (to be considered as a lower bound) and the simulated momentum flux (also to be considered as a lower bound). The balloon zonal and meridional momentum fluxes indicate phase lines such that the wave vector is oriented along the northwest-southeast direction. This is compatible with the orientation of some of the wave packets present in the simulation. It is also worth noting that a clear signal for a lower frequency wave packet (intrinsic period between 6 and 8 h, corresponding to intrinsic frequency between 1.8 and 2.4 f at 55°S) is present during the whole time of passage above the tropospheric low-pressure system. Its instantaneous contribution to momentum fluxes is smaller, but is nonetheless of the order of 5 mPa, and it extends over a larger area.

Two other balloons, #8 and #22, come in the vicinity of the region of enhanced gravity wave activity on day 320, as indicated in Figure 3. Balloon #8 does not detect any enhancement of momentum fluxes, and balloon #22 detects a moderate wave packet of low frequency, with associated momentum fluxes of about 5 mPa (Figure 6, right). The apparent disagreement for balloon #8 confirms that there is some uncertainty in the location of the simulated wave packet, which is evident and illustrated by the sensitivity to the choice of initial time in Appendix A.

3.3. Background Flow in the Troposphere and Lower Stratosphere

In the region on which we focus, over the Southern Ocean, an intense low-pressure system forms during day 319 (15 November 2005), with a clear surface temperature front, oriented from northeast to southwest. The low-pressure system and the front are clearly identified also in surface temperature and vorticity, as shown in Figure 7. Two nearby low-pressure systems are present during the period, both of rather small dimensions (about 500 km in diameter) and moderately deep (975 hPa on day 319.75 for the low of interest here, located near 60°S and 103°E). The dimension suggests that these are polar lows. Intense surface winds are often associated with polar lows and are indeed present equatorward of the low (~18 m s^{-1} for winds at 10 m height, not shown).
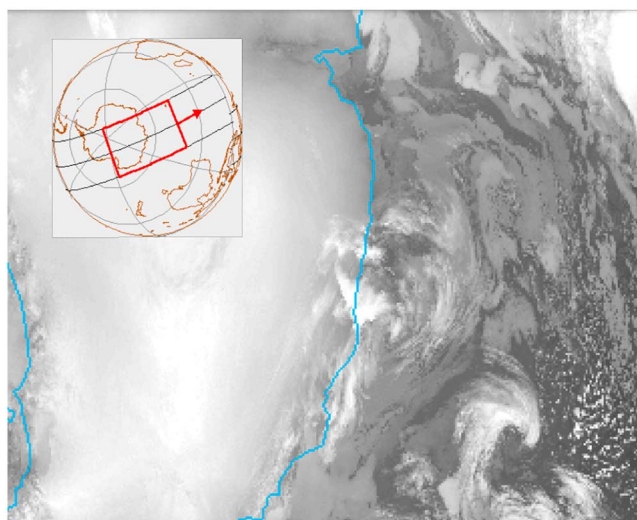
Figure 8. Satellite image for the infrared channel, day 319.49 (11:50 UT), from the Defense Meteorological Satellite Program, along with the orbit track and angle of view inserted in the upper left. Note the conspicuous clouds, with a comma shape indicative of cyclonic rotation, to the lower right of the figure. This is to be compared with Figures 7 and 3 (right).

In the midtroposphere, the flow near 100°E blows toward the southeast, as depicted by the pressure field shown in Figure 3 (right). Maximum wind speeds are typically between 25 and 30 m s^{-1}. On the poleward side of this jet, one finds intense, localized updrafts (up to 0.4 m s^{-1}). These are located in the vicinity of the low, about 100 km ahead of the front as identified in the surface vorticity. The reality of the polar low and associated convection is confirmed by inspection of satellite images; see Figure 8.

Also shown in Figure 3 is a contour for ice content at the same level, showing a local maximum of ice content coinciding with the strong localized updrafts attached to the polar low. One should note, however, that much more extended regions of significant ice content are present in other locations, generally associated with weaker updrafts in a broader region. At time 319.75, one recognizes clearly the same cyclonic signature in the structure of the surface front and in the updraft above, as well as in Figure 8.

In the lower stratosphere, the major feature of the flow is the transition from the tropospheric jet stream to the stratospheric polar vortex (see Figure 3). As can be seen from the pressure lines in Figure 3 (left), the polar vortex is significantly displaced away from the pole. Investigation of the temperature in the lower stratosphere reveals regions of sharp gradients consistent with the shear needed for the transition between the tropospheric jet streams over the Southern Ocean and the stratospheric vortex above Antarctica.

3.4. Generation Mechanisms

It is not straightforward to identify the generation mechanisms for wave packets in such complex flows. As seen in Figure 3, one does not see precisely one wave packet appearing at a precise time. Rather, there is a region of more important wave activity, more or less intense, more or less organized, during the whole of day 319, and the proximity to the simulation domain boundary makes it difficult to trace the wave packet much further backward. Nonetheless, several features are clear and suggestive.

In the course of day 319, a more intense wave packet comes out, particularly clear around day 319.75. At the surface, a polar low is present, with well-defined fronts and intense, localized updrafts ahead of the front.
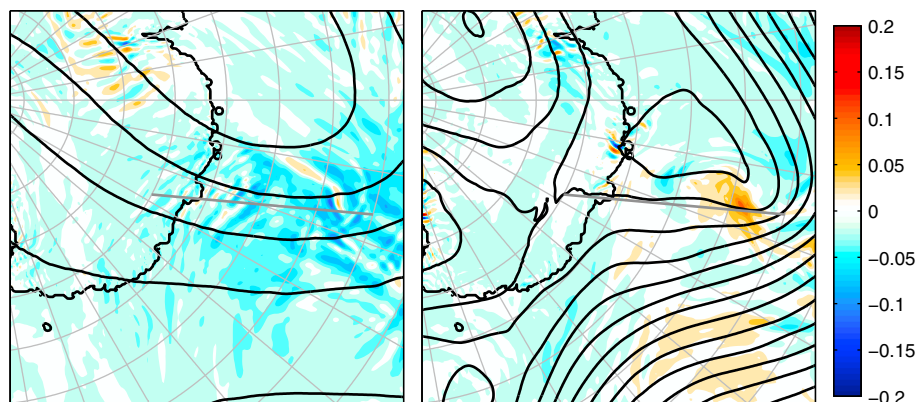

Figure 9. Vertical velocity at altitude (left) $z = 20$ km and (right) $z = 5$ km in the dry simulation for day 319.75, to be compared with the middle panels of Figure 3.
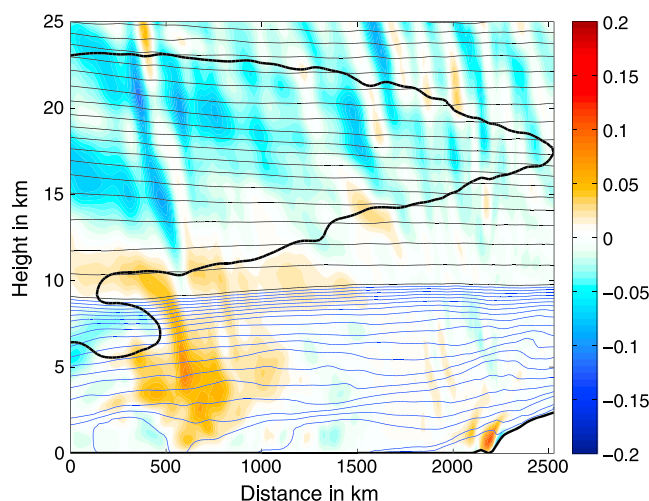
Figure 10. Vertical cross section of the vertical velocity in the dry simulation for day 319.75, to be compared with Figure 4 (middle).

Typical of convection at such latitudes, the updrafts extend to about 6 km altitude. In the lower stratosphere, the flow changes, with the polar vortex being displaced in such a way as to yield strong poleward winds above the polar low. The main wave packet we focus on is found downstream of the tropospheric updrafts (downstream being taken relative to the stratospheric winds). It has characteristics that differ from those expected by theoretical studies of spontaneous emission, as its intrinsic frequency is rather high (close to $10 f$, rather than between f and $2 f$). All these elements and the vertical cross sections shown in Figure 4 suggest that the convection tied to the polar low is partially responsible for the intensity and the characteristic of the waves.

In order to test the importance of moist processes in the generation of the gravity waves, a "dry" simulation was carried out: the heating from the microphysics parameterization and the parameterization of cumulus convection are both turned off. The comparison of the dry and the full simulation brings further evidence for the role of moisture. As seen in Figures 9 and 10, the intense tropospheric updraft associated to convection is replaced by a broader region of much weaker positive vertical velocity, and at stratospheric heights the wave activity is considerably weaker. Some waves are still present, with details comparable to those of the background waves present in the full simulation. Conspicuously absent is the clear, relatively intense wave packet which is responsible for the peak in momentum fluxes.

4. Case Study 2: Days 313 and 314

The second case study presented is complementary to the first one in several ways. Whereas the first case consisted in a localized event with only few, fairly identifiable wave packets, the second case has a broader region of scattered wave activity (section 4.1). Here we use the vertical profile information available from satellite to compare cross sections of HIRDLS measurements to the model. Whereas the first case was tied to a polar low at the surface, the second occurs when a deep, synoptic low is passing over the region, with a marked front extending more than a thousand kilometers (section 4.3). Yet similar elements of the flow appear associated with the generation of the gravity waves (section 4.4). Finally, the sensitivity to resolution is described in section 4.5.

4.1. Modeled Gravity Waves

A broad region of gravity wave activity is found at altitude $z = 20$ km during day 313 and until day 314.50. As illustrated in Figure 11, several wave packets are present, with phase lines generally oriented transverse to the flow, although there are significant variations. The description of this wave event again covers two simulations: a first one started on day 311.00 (7 November, 00:00 UT) and ending on day 314.00 and the second one started on day 313.00 (9 November, 00:00 UT) and ending on day 316.00.

The region of enhanced wave activity is fairly close to the coastline and moves over the continent by day 314.50. For that date, one should be careful to distinguish a contribution from orographic waves above the Antarctic coastline. Vertical cross sections are particularly helpful for that purpose, as shown in Figure 12. One again finds the clear signature of convection in the troposphere, located ahead of the surface front. Strong updrafts in the troposphere (of the order of 0.5 m s^{-1}) connect to extended regions with gravity waves present in the lower stratosphere. These extend downstream, in regions where the local stratospheric winds are strong (>30 m s^{-1}). Within the region where gravity waves are present, several wave packets
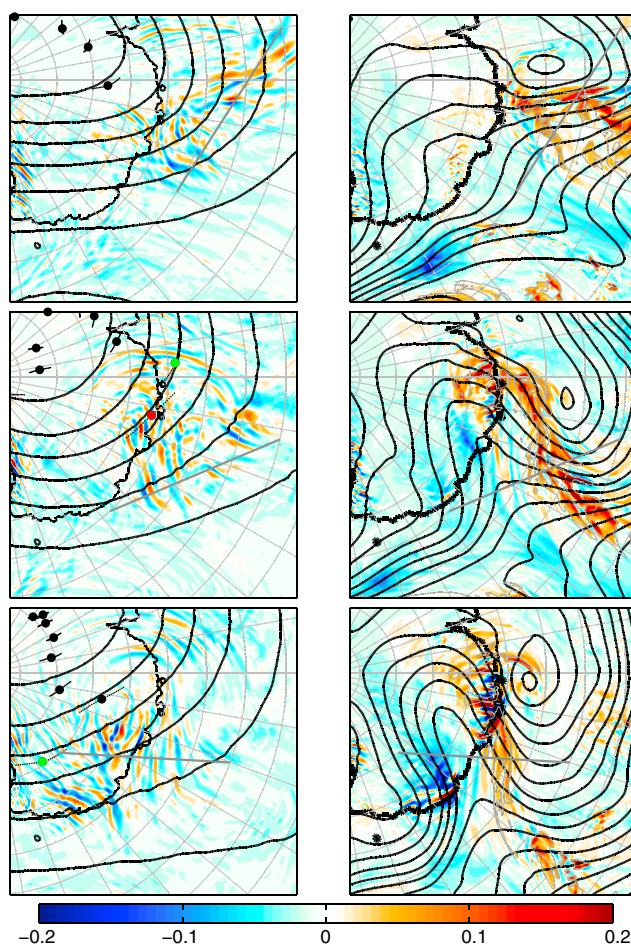
Figure 11. Horizontal maps of w (colors, in m s^{-1}) for days (top) 313.00, (middle) 313.75, and (bottom) 314.50 at (left) $z = 20$ km and (right) $z = 5$ km, as in Figure 3. Highlighted balloons are #26 (red) and #27 (green).

which seem more intense than others come out (e.g., in Figure 12 (middle), at along-section distances of ~1000 km and 2000 km).

The analysis of the wave characteristics has focused on such wave packets as they could be clearly identified. For each, the wavelengths were estimated at an altitude of 20 km, yielding an estimate of the intrinsic frequency. Eleven wave packets were thus analyzed. The mean horizontal wavelength was 190 km, with spread between the different wave packets from 120 to 280 km, such that the waves may be considered generally well resolved (horizontal wavelengths of ~10 Δx, i.e., 200 km). The vertical wavelengths range from 4.5 to 8 km, with an average of 6 km, yielding intrinsic frequencies that are of the order of 5 f. In other terms, the wave packets that contribute most to the momentum fluxes are not near-inertial.

Momentum fluxes for this event were calculated from the simulations and found to be large over an extended region during the whole of day 313. When fluxes are spatially averaged in boxes 10° longitude by 5° latitude, values of 4 mPa or larger are commonly found over the ocean, with a maximum of 7 mPa on day 313.75. During day 314, as the region of wave activity moves over the coastline, narrower regions of intense fluxes are found over the coastline, with orography playing a role in the generation.

4.2. Observed Gravity Waves

The comparison to observations is carried out relative to satellite observations. During day 313, 4 swaths are available in the region of interest, shown in Figure 13. The satellite takes 8 min to cover the distance indicated, and the times corresponding to the center of the portions shown for the four swaths are 10:04, 11:40, 13:14, and 14:51 UT.
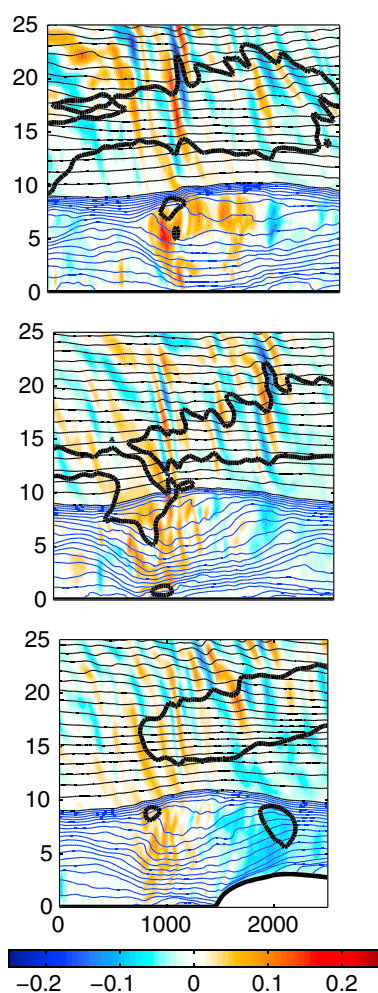
Figure 12. Vertical cross sections of the vertical velocity (colors, in m s^{-1}) for times (top) 313.00, (middle) 313.75, and (bottom) 314.50. Also shown are isentropes (blue lines with contour interval 2.5 K up to 320 K, black lines with contour interval 20 K above that), and the isotach for $|\mathbf{u}| = 35$ m s^{-1} (thick black line). The locations of the vertical cross-sections are presented in Figure 11. Coordinates are shown in kilometer.

There are several difficulties in retrieving gravity wave signature in the satellite observations for these swaths: (1) because of the displacement of the polar vortex, the background flow is quite complex and the removal of a background to identify the gravity waves is not straightforward; (2) it is expected from the simulations that the gravity wavefield is fairly complex, with several wave packets having various orientations; and (3) the resolution of the observations makes the analysis of waves with horizontal wavelengths on the order of 200 km delicate. An overview of the limitations due to viewing geometry and observational filter for the retrieval of gravity waves from limb sounding observations can be found in *Preusse et al.* [2009]. These difficulties make a precise, quantitative comparison difficult.

From the horizontal cross section of the vertical velocity shown in Figure 13, we expect to find two major regions of gravity wave activity, one near 120–125°E and one near 100–105°E. Henceforth, we focus on two swaths, numbered 2 and 4 in Figure 13. The cross sections of the temperature obtained from these swaths are shown in Figure 14 and are to be compared with the equivalent cross sections shown in Figure 15 for the simulations. Four remarks need to be made. First, the plots differ by their horizontal resolution: in the simulations, we have not degraded the resolution, whereas the observed profiles are on average spaced 91 km apart. Second, in the simulations, the output above 30 km is affected by the presence of the model top (at 5 hPa, near 36 km) and hence should not be considered for the comparison. Third, limb sounding inherently averages a measured signal along the line of sight over a distance of roughly 100–150 km due to the averaging kernel effect [*Gille et al.*, 2008; *Preusse et al.*, 2009], and we have not modeled this effect in the comparison. Finally, it has been checked that the choice of the polynomial fit used to separate the temperature into a background and a perturbation only weakly influenced the perturbation signal for heights larger than about 15 km.

The overall structure of the temperature field agrees very well between observations (Figure 14, left) and simulations (Figure 15, left). It bears a strong signature of the displacement of the polar vortex away from the pole. Horizontal perturbations were obtained by removing a parabolic fit to the temperature variation at each height, both for the observed and simulated cross sections.
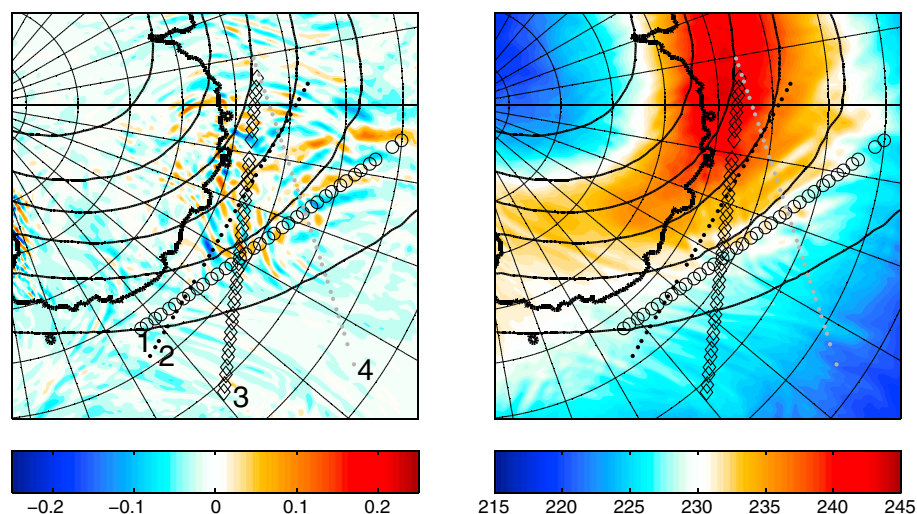
In both observations and simulations, a region of significant small-scale perturbations is clearly present, at the edge of the polar vortex. In the observed sections of Figure 14, one can identify wave patterns, with a fairly well-defined slope corresponding to low-frequency waves. Because of the limited spatial resolution, the wave pattern is only partly described, and the amplitude is underestimated. Remarkably, similar wave patterns are present in the simulated sections of Figure 15. They are embedded in a set of several wave packets, with higher-frequency waves also present (steeper slopes). For the low-frequency component, the amplitudes are comparable, though somewhat larger in the simulations than in the satellite observations (fluctuations of the order of a couple of Kelvins).

As shown in Figure 11, two balloons, #26 and #27, fly in the region of interest. However, they come into the region of wave activity when and where this region is above the coastline. Gravity waves that are sampled by the balloons result from the complex interaction between the frontal system and the orography and are outside the scope of the present study. Hence, they are not discussed.

Figure 13. Maps of (left) vertical velocity (in m s^{-1}) and (right) temperature (in K) at altitude $z = 20$ km, for day 313.50. Overlaid are the four swaths from HIRDLS that are going through the region of interest, numbered 1 to 4 in Figure 13 (left).

4.3. Background Flow in the Troposphere and Lower Stratosphere

In contrast to the previous case, the tropospheric flow is dominated by a large-scale low-pressure system that is more comparable to midlatitude lows. A broad low-pressure system comes into our domain of interest at the end of day 312, moving slowly eastward. The pressure minimum in region A reaches about 942 hPa on day 314.25. Associated to the low-pressure system is a front that is well identified in surface vorticity (see Figure 16). At the beginning of day 313, it is oriented north-south, but the front progressively moves to an orientation that is more northeast-southwest during the day.
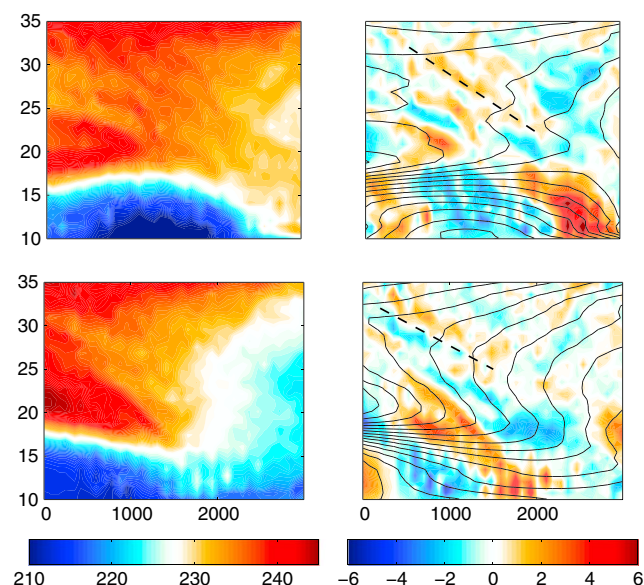

Figure 14. (left) Observed temperature and (right) temperature perturbation with overlaid black contours of the background temperature from the HIRDLS data for swaths (top) 2 and (bottom) 4, in Kelvin. Horizontal coordinate is the distance in kilometer along the swath, and vertical coordinate is altitude in kilometer. The dashed lines in Figure 14 (right) indicate slopes for near-inertial waves (6.7 10^{-3} and 5.4 10^{-3} for Figures 14 (top) and 14 (bottom), respectively).

Maps of the vertical velocity in the midtroposphere are shown in the right column of Figure 11. Two points are worth noting: as shown by the pressure field, a strong jet is positioned above the surface front, with a jet exit region present just downstream of the front. This region of diffluence is similar to the one highlighted in studies that found significant waves in jet exit regions [see *Plougonven and Zhang*, 2014, and references therein]. The second point is that significant convection develops during day 313, with a clear signature of localized intense updrafts (up to 0.35 m s^{-1}) located all along the front at day 313.75.

4.4. Generation Mechanisms

Some elements appear to be common with case 1 (day 320), while others differ. Differences include the surface pressure pattern and the tropospheric flow. In the present case, a deep large-scale low-pressure system is present, with a well-identified front extending over 1000 km. The front is located between a trough and a ridge of surface pressure.
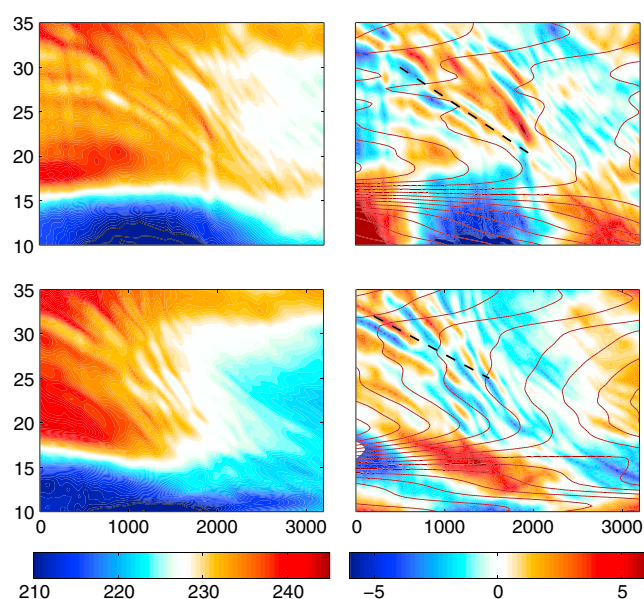
Figure 15. (left) Simulated temperature and (right) temperature perturbation (in K) with overlaid black contours of the background temperature from the WRF simulations, along the same sections as Figure 14. Horizontal and vertical coordinates are given in kilometer.

Above the front, strong winds are present, with a conspicuous jet exit region present downstream. Differences also include the extent of the region of enhanced gravity wave activity in the lower stratosphere. Similarities include the presence of significant updrafts in the midtroposphere associated to convection ahead of the surface front. Similarities also include the position of the stratospheric vortex, such that the region of enhanced gravity waves is again embedded in the region of strongest wind at that height (>45 m s^{-1}).

Vertical cross sections again suggest a connection between the convection tied to the surface front and the waves aloft and downstream, though the connection is not as clear as in case 1. One reason certainly is the greater complexity of the wavefield in the present case, suggesting different mechanisms are acting in combination. To assess quantitatively the importance of moist processes, a dry simulation was carried out, as for case 1.

Figures 17 and 18 show horizontal and vertical cross sections of vertical velocity in the dry simulation, to be compared with Figures 11 (middle) and 12 (middle). Again, the gravity wave activity is much weaker, with the more conspicuous wave packets being much attenuated, but not altogether absent. This provides further evidence that moisture plays a significant role, if not as the direct source of the waves, at least as a factor amplifying them and shaping their characteristics. The importance of moist processes is more thoroughly and systematically evaluated in section 5.

4.5. Sensitivity to Resolution
A simulation with double resolution in the horizontal ($\Delta x = 10$ km) has been carried out for the present case. Horizontal maps of the vertical velocity at $z = 5$ and 20 km are shown in Figure 19. As expected, the resolution has a significant impact on the vertical velocity field, which is known to be very sensitive. A wealth of details that were unavailable at low resolution now appear, but the amplitudes of the updrafts away from the orography are only marginally enhanced (about 20%). Moreover, the organization and main features of the vertical velocity field are unchanged. In other words, one does not find a significant qualitative change as resolution is increased from $\Delta x = 20$ km to $\Delta x = 10$ km. The impact for momentum fluxes is discussed in section 5.2.

5. Discussion

The above sections have put forward a number of results based on two case studies. In particular, the role of moisture and a good agreement between simulated and observed gravity wave activity have been emphasized. Now, the simulations without moist processes and those with double resolution are available on a domain much wider than region A on which these case studies focused. In addition, we have standard simulations that extend for a much longer period of time (58 days; see section 2.1) than the two sequences of 2 days that have been described above. Below we use the rest of the domain and the other simulations to investigate more systematically the enhancement of the gravity wavefield in the presence of moist processes (section 5.1), the sensitivity to resolution (section 5.2), and the mean orientation of the gravity waves (section 5.3).
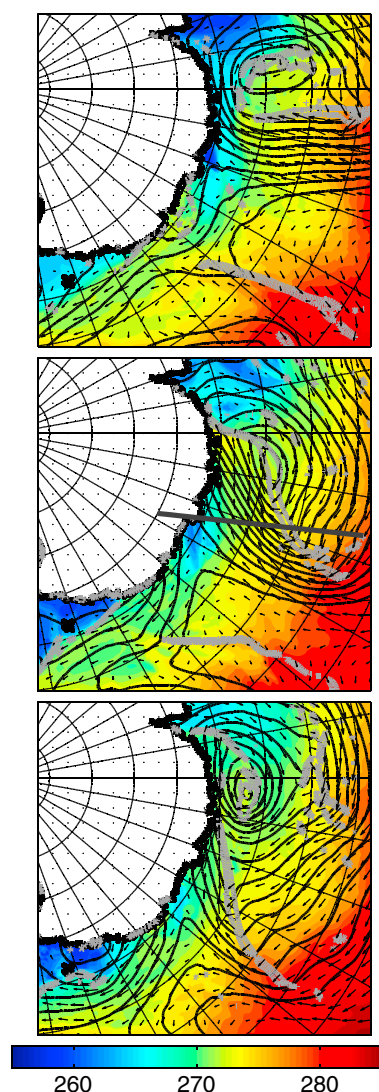
5.1. On the Importance of Moist Processes

The case studies presented suggested that moist processes contributed significantly to the generation of gravity waves. This is not an unexpected result. Case studies involving numerical studies have already emphasized that moist processes could contribute to enhancing waves [e.g., *Zhang et al.*, 2001]. There are several ways in which moisture can contribute. Moisture is known to enhance the growth of baroclinic instability [*Waite and Snyder*, 2012; *Lambaerts et al.*, 2012], and this in itself can be expected to enhance gravity waves [*Wang and Zhang*, 2007]. However, this would be expected to produce only an enhancement, not a qualitative change as the one that can be seen comparing Figures 4 and 10 (absence of the localized updrafts in the troposphere and of the more intense waves in the stratosphere). The moderately high intrinsic frequencies ($5–10 f$, with f as the Coriolis parameter) and the comparison of these cross sections suggest that moisture plays a more direct role in the excitation of waves than simply enhancing the development of the baroclinic instability.

Now to more systematically quantify the contribution of moist processes, the momentum fluxes in the full and in the dry simulations are compared for all output times corresponding to cases 1 and 2 for which dry simulations are available. For each output (every 6 h), momentum fluxes have been calculated and averaged in boxes 10° longitude by 5° latitude, for the whole domain. Only boxes over the Southern Ocean are retained, corresponding to region 5 of PHG. Figure 20 shows scatterplots comparing the momentum fluxes plotted separately for each episode (days 312 to 313.75 on the left, days 318 to 321.75 on the right). A log-log plot is chosen because of the distribution of the values of momentum fluxes, with many weak values and a few large values. In this format, a proportionality factor between the two data sets shows as a vertical offset. In both cases, the momentum fluxes in the dry simulations are generally weaker. A linear regression yields a slope of 0.39 in one case and 0.40 in the other. The serendipitous closeness of these two coefficients should not suggest that the value of two fifths is particularly meaningful. Nonetheless, it is likely robust to expect that momentum fluxes in simulations including moisture are at least twice as large as their counterparts in dry simulations.

Figure 16. Maps of surface temperature (in K) and vorticity as in Figure 7, but for days 313, 313.75, and 314.50.

Further comparisons were also made using all days for two additional dry simulations corresponding to earlier times (days 294–298). The momentum fluxes in these dry simulations were about one fifth of those in the corresponding full simulations. The reasons for this sharper difference are beyond the scope of the present study, the main point is that these additional simulations do not contradict our conclusions, on the contrary.

Similar comparisons were made for orographic regions (Antarctic Peninsula, Antarctic coastline). The momentum fluxes were generally very comparable in both the dry and standard simulations with linear regression yielding slopes close to 1, except for days 318–321 above the Antarctic Peninsula. For these days the momentum fluxes above the Antarctic Peninsula differed both qualitatively and quantitatively, the dry fluxes being larger by a factor 1.5 on average. Now it is known that orography can strongly impact convection [e.g., *Kirshbaum and Durran*, 2003], so it is not expected that the gravity waves should be identical over orography. However, the impact of moist processes can follow several paths (changes of wind or stratification upstream, direct excitation of GW by convection above the orography) so it is not expected to be systematic. Inspection of the simulations in the present case suggests that convection upstream of the Antarctic Peninsula has modified the wind pattern sufficiently (local differences up to 4 m s^{-1}, although the
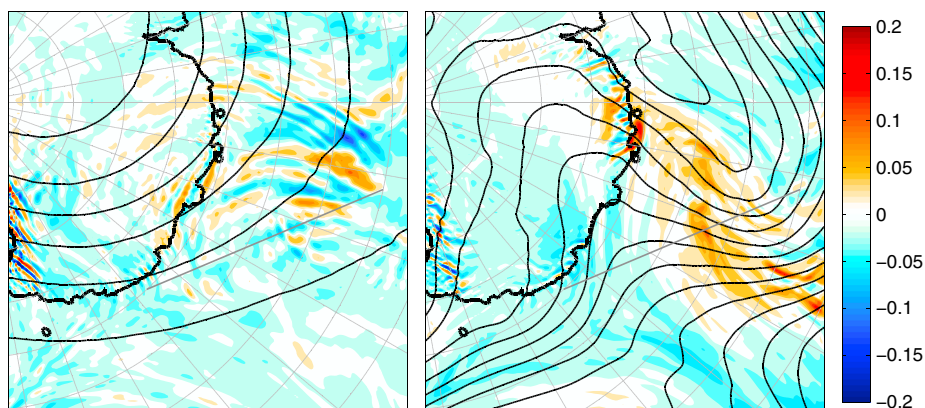
Figure 17. Vertical velocity in m s^{-1} at altitude (left) $z = 20$ km and (right) $z = 5$ km in the dry simulation for day 313.75, to be compared with Figure 11 (middle).

general wind pattern is very similar) that the gravity wave response to the Peninsula differs significantly, with a stronger response in the dry simulation.

Sensitivity to the choices of parameterizations for the microphysics and for the convection have not been tested. The necessary use of parameterizations certainly introduces uncertainty in the simulated gravity waves and calls for further study. *Stephan and Alexander* [2014] have investigated specifically the sensitivity of modeled gravity waves to physics parameterizations, for a summer squall-line over the Great Plains with a resolution down to d$x = 1$ km. Encouragingly, they found weak sensitivity of the emitted gravity waves to different choices of physics parameterizations. It is, however, not evident that this result applies in the present case, as the context and resolution are very different.

The above comparisons between the dry and the full simulations bring evidence that the differences noted in sections 3 and 4 are likely significant and representative of a significant underestimation of momentum fluxes in dry simulations of midlatitude jets and fronts. The present simulations with the moist processes parameterized and the sensitivity to resolution (see below) unfortunately do not allow to conclude on the relative contributions from moist convection and from dry frontogenesis.

5.2. On the Sensitivity to Resolution

Both comparisons of simulated waves, with balloons and with satellite observations, proved rather satisfactory but had notable limitations. Indeed, the simulations were found to be sensitive to resolution (section 4.5); the balloon measurements had a temporal resolution which only allowed to describe waves with intrinsic periods larger than 1 h. The vertical profiles of temperature obtained from HIRDLS are spaced about 100 km apart, making it possible to resolve only wave patterns with wavelengths of 200 km or greater, with appropriate orientation, so that we restricted to a qualitative comparison above. Below we discuss how much underestimation of the gravity waves can be expected from the simulations and from the balloon measurements.

Figure 18. Vertical cross section of the vertical velocity in m s^{-1} for day 313.75 in the dry simulation, to be compared with Figure 12 (middle). Contours and color range are the same to allow comparison.

The Vorcore balloons only recorded measurements every 15 min, so that waves with high intrinsic frequencies (periods shorter than 1 h) were not resolved. At high latitudes, the inertial period is close to, and somewhat larger than, 12 h, and in the lower stratosphere,
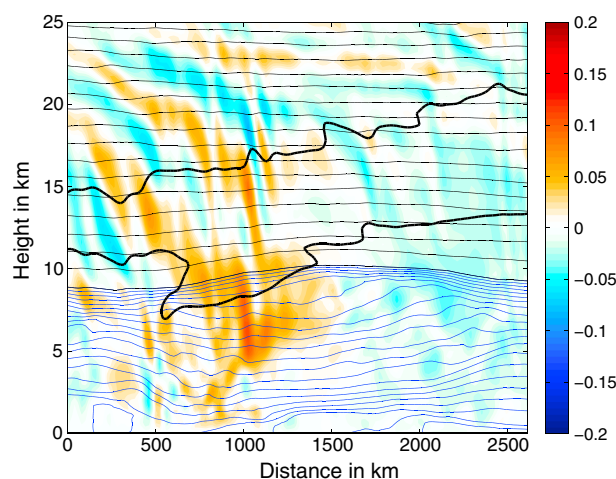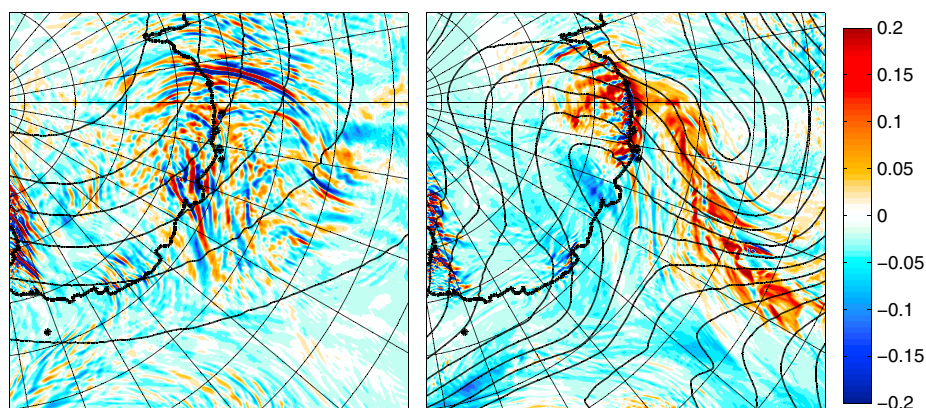
Figure 19. Simulated vertical velocity in m s^{-1} at $z = 20$ (left) and 5 km from the high-resolution simulation ($\Delta x = 10$ km), to be compared with Figure 11 (middle) (the color range is the same).

the buoyancy period is close to 5 min. There is therefore approximately a factor 12 between the inertial period and the shortest resolved period in the Vorcore balloon data set, and another factor 12 between this shortest resolved period and the buoyancy period. Now the spectral density of momentum fluxes scales as $\hat{\omega}^{-1}$ [*Hertzog and Vial*, 2001], so that it is expected that only half the momentum fluxes are resolved by the Vorcore balloon measurements. In other words, the Vorcore balloon measurements are expected to underestimate momentum fluxes by a factor 2 because of the temporal resolution of these measurements. Future investigation of the momentum fluxes from superpressure balloons with higher temporal resolution will prove very informative regarding this issue. Preliminary results from the Concordiasi campaign suggest that the momentum fluxes over the ocean were underestimated from the Vorcore measurements by a factor 2 to 3 (A. Hertzog, personal communication, 2014).

For the simulated momentum fluxes, the sensitivity of the momentum fluxes to the spatial resolution was tested with runs at a doubled horizontal resolution ($\Delta x = 10$ km). In PHG, the sensitivity to resolution was investigated based on 6 days using a doubled resolution. Momentum fluxes at an altitude of 20 km were found to be twice as large in the high-resolution simulations. The high-resolution simulation carried out for case 2 (section 4.5) was not among those simulations and hence constitutes a new opportunity to test the sensitivity to resolution. The momentum fluxes were calculated as in PHG and compared, for 2 days of output and over the ocean (region 5 of PHG), between the standard and high-resolution simulations. As expected, the fluxes were larger in the latter case, but the linear regression yields a slope of 1.4, not 2 as in PHG. This confirms the expected sensitivity to resolution. Indeed, the sensitivity to resolution is always an important issue with simulations of gravity waves, whether for waves generated by dry, idealized fronts
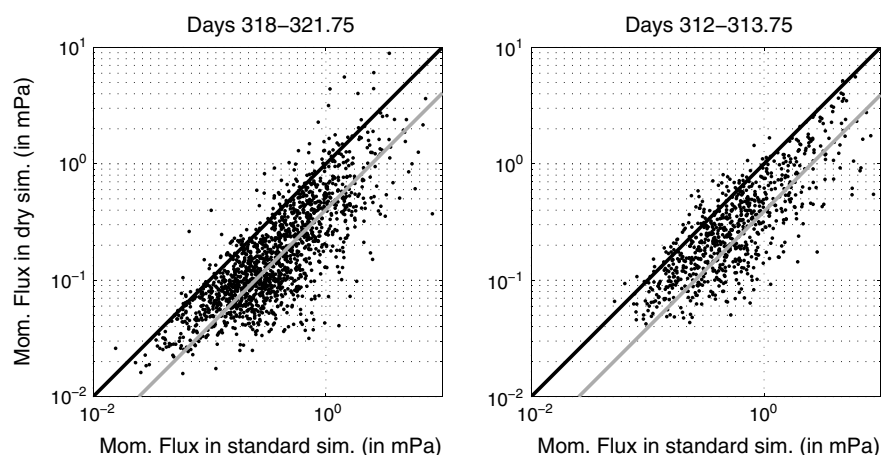

Figure 20. Scatterplot of the momentum fluxes in the standard and dry simulations (horizontal and vertical axes, respectively), averaged in boxes $10° \times 5°$, for (left) case 2 and (right) case 1.
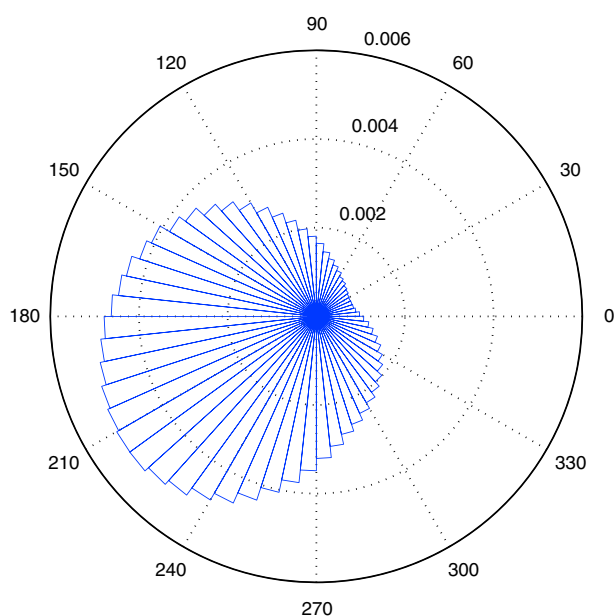
Figure 21. Probability distribution function of the angle made by the momentum fluxes, in the 2 months of WRF simulations carried out in PHG. Only locations above the Southern Ocean and with momentum fluxes larger than 1 mPa are considered. See text for details.

[*Zhang*, 2004], or by convection [*Chagnon and Gray*, 2008; *Kim and Chun*, 2010; *Jewtoukoff et al.*, 2013]. In the case of convectively generated waves, studies have rather focused on tropical convection and have highlighted a sensitivity to resolution in grids much finer than the one presently used [*Lane and Knievel*, 2005], i.e., below $dx = 1$ km. In other words, the simulations do not allow a conclusive estimation of the amplitude of the fluxes, and comparison to observations will remain crucial even as the resolution of simulations increases. Further investigations of gravity waves emitted from jets and fronts with simulations having significantly higher resolution (at least $dx \sim 1$ km, so that moist convection does not need to be parameterized) will prove very informative on this issue.

5.3. On the Orientation of the Waves

In the comparison of the simulated waves with those described in satellite observations, two limitations of the latter were discussed: resolution and orientation of the swath. The latter is further discussed here. At high latitudes, the satellite swaths are essentially zonal (exactly zonal at the turnaround latitude, 64°S in the Southern Hemisphere). It matters to determine how anisotropic the wavefield is, in order to know how appropriate these satellite observations are to estimate gravity wave disturbances. For example, the meridional orientation of the wave vector in case 1 made the satellite observations inappropriate to detect the waves, contrary to case 2. The whole 2 months of simulations that were carried out in PHG are now used to assess the preferred orientation of gravity waves over the Southern Ocean.

Figure 21 shows the probability distribution function (PDF) of the orientation of momentum fluxes due to small-scale perturbations (see PHG for details on the calculation) over the Southern Ocean between 50°S and 65°S (region 5 of PHG: this is restricted to areas above the ocean only, far from orographic features such as the Antarctic Peninsula, the tip of South America, and small islands). Only locations where momentum fluxes were larger than 1 mPa were retained, and all 6-hourly outputs were used, covering 58 days from 21 October, 00:00 UT, to 18 December, 00:00 UT. The radius of the bars indicates the probability for the fluxes to be in a certain angular sector, with the angles in degrees. The momentum fluxes show a very clear preference for an orientation toward the southwest. The maximum of the PDF is for an angle of −141° relative to the east. This orientation is 6 times more probable than the least probable orientation (27°). When a threshold higher than 1 mPa is used, the anisotropy is yet enhanced. If the orientation of the waves is analyzed from the time-averaged momentum fluxes, the anisotropy becomes much more pronounced: 42% of the fluxes have an orientation in a 30° sector around the mode of the distribution (−159° for the time-averaged fluxes).

In consequence, HIRDLS observations are very well suited for the analysis of gravity wave perturbations at high southern latitudes. The mainly zonal orientation of the swaths should allow to capture the major part of the wave signatures. The investigation of a potential asymmetry between wave amplitudes in the ascending and descending parts of the swaths may confirm the preferred orientation found in the simulations.

6. Summary and Conclusion

The present study described two case studies of intense gravity wave events over the Southern Ocean, using both mesoscale simulations and observations. The goals were to assess the ability of the mesoscale model

to reproduce nonorographic wave events and to identify flow configurations and wave packets conducive to significant momentum to the stratosphere. The simulations used the *Weather Research and Forecast Model* (WRF) [*Skamarock et al.*, 2008] at a horizontal resolution of $\Delta x = 20$ km, as described in *Plougonven et al.* [2013]. The observations consisted of in situ measurements from superpressure balloons in the lower stratosphere from the Vorcore campaign [*Hertzog et al.*, 2007, 2008] and remote-sensing measurements of the temperature by the HIRDLS instrument [*Alexander and Barnet*, 2007].

The first finding is the good agreement between the simulations and the observations and the estimation of the momentum fluxes associated to nonorographic wave events. For case 1 (section 3), both the simulated fluxes and those calculated from balloon measurements describe a localized wave packet with maximum momentum fluxes of about 30 mPa, extending over a region of a few hundred kilometers. For case 2, the low-frequency (large-scale) part of the wave activity described in the simulations is detected in the satellite observations, with very similar tilt for the phase lines (hence intrinsic frequency) and comparable amplitudes for the temperature anomaly. The limited horizontal resolution of the satellite observations, combined with the complex background (strong gradients due to a displaced polar vortex) and the complexity of the gravity wavefield itself precludes a more quantitative comparison, e.g., for wavelengths. These comparisons are encouraging results justifying further use of the simulations to explore the generation of nonorographic waves. These case studies and the discussion on the underestimation of the momentum fluxes (section 5.2) suggest that such nonorographic wave events may be typically associated to fluxes of order 50 to 100 mPa. In fact, nonorographic wave events accounting for fluxes of several tens of mPa have been found in high-resolution ECMWF analyses by *Preusse et al.* [2014] and can even contribute significantly to hemispheric gravity wave momentum fluxes for single days.

The second finding consists in the emphasis on moist processes playing a role in the generation and amplification of gravity waves. Interestingly, this emphasis comes out of both case studies, despite considerable differences between the tropospheric flows involved: a polar low in case 1 (section 3.3) and a deep, large-scale synoptic system in case 2 (section 4.3). Evidence for the role of moisture came from conspicuous convective updrafts present below and upstream of the main stratospheric wave packets and from the comparison of the full simulations with dry simulations, from which these conspicuous stratospheric wave packets were absent.

The third finding is the relatively high intrinsic frequencies of the waves (between 5 and 10 f). This is in contrast with the emphasis on low-frequency inertia-gravity waves from idealized studies [*Plougonven and Zhang*, 2014, and references therein]. The two findings above are of course connected: convection, although considerably weaker of course than in the tropics, directly forces vertical motion, over a rather deep portion of the troposphere (typically 6 km here), and hence favors the excitation of waves with higher frequencies than spontaneous emission from dry, balanced motions.

Two remarks are in order concerning these two last findings:

1. The emphasis on moist processes and higher frequencies comes in part from the criterion used to identify the case studies (i.e., strong momentum fluxes at $z = 20$ km). In idealized simulations of baroclinic life cycles, waves were rather investigated from signatures in the divergence field near the tropopause [e.g., *Plougonven and Snyder*, 2007], favoring the detection of lower frequency wave packets.

2. The role of moisture is here emphasized because it was somewhat unexpected at such high latitudes, but this should not overshadow that significant fluxes are also found in the dry simulations. The systematic comparison of the full and the dry simulations over oceanic regions showed that momentum fluxes in the latter case were 2.5 times weaker. This is a significant factor, implying that moisture needs to be taken into account in further theoretical investigations, as in *Waite and Snyder* [2012], *Wei and Zhang* [2014], and *Mirzaei et al.* [2014]. Given that moist processes are parameterized in the present simulations, this factor is only indicative and should be taken with caution. Further investigations are needed to quantify the role of moisture in nonorographic wave generation at middle and high latitudes.

Finally, we wish to highlight several issues that call for further examination:

1. *The estimates of momentum fluxes* were found to be in satisfactory agreement between the model and balloons. This is very encouraging. At the same time, the simulations were found to remain sensitive to
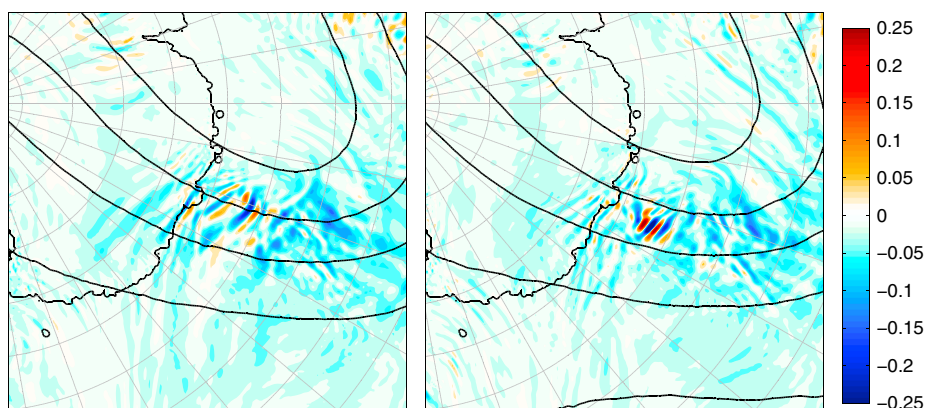
Figure A1. Vertical velocity in m s^{-1} for day 320, 00:00 UT (left) from the simulation started on day 317, 00:00 UT, and (right) from that started on day 319, 00:00 UT.

resolution (section 5.2). The two can be reconciled given that the balloon estimates are also expected to underestimate the momentum fluxes, because the temporal resolution of the measurements did not allow to describe the whole spectrum of gravity waves.

2. *Wave capture* [*Bühler and McIntyre*, 2005] has been emphasized in theoretical studies [e.g., *Plougonven and Snyder*, 2005; *Wang and Zhang*, 2010], and its presence in the flows simulated here remains to be investigated. As suggested above, investigating the gravity wavefield from a different angle may highlight different components of the wavefield.

3. *Strong shear* was present in both cases between the troposphere and the lower stratosphere. The waves were found to be present in regions of strong stratospheric winds. The importance of shear has been highlighted in theoretical studies depicting the coupling of balanced motions and gravity waves [e.g., *Lott et al.*, 2010]. Further investigation of the role of shear (e.g., Are there cases of strong convection without gravity wave signatures aloft?) may provide insights to better understand nonorographic wave generation.

On a number of these issues, the Concordiasi field campaign which involved 19 superpressure balloons over Antarctica in austral spring of 2010 [*Rabier et al.*, 2010] may bring significant elements of answer. Indeed, the temporal resolution of the balloon measurements was significantly enhanced relative to Vorcore, allowing a full description of the gravity wave spectrum. The relative contributions of high- and low-frequency waves above the oceans can therefore be quantified in this data set, contributing to a more complete estimation of momentum fluxes and a better understanding of the relative roles of different components of the gravity wave spectrum.

Appendix A: Sensitivity to the Forecast Time

As stated in section 2.1, the simulations were run for 3 days each, with the first day serving as spin-up. We here present for case 1, for illustration, how similar the wave packets are in the two runs that overlap from day 319.00 to 320.00. The second simulation, started on day 319.00, is considered mature for analysis after 24 h of spin-up, i.e., on day 320.00.

Maps of the vertical velocity are shown in Figure A1. The pressure fields are nearly indistinguishable, but there are significant differences between the wave packets described in both simulations; the contrary would have been very surprising. However, if we restrict to the broad characteristics of the wavefield, both forecasts agree in simulating a local maximum between 50 and 65°S, and between 105 and 120°E, with maximum vertical velocities of 0.15–0.25 m s^{-1}, wavelengths of order 100–150 km and phase lines normal to the local flow. In the 3 day forecast, the waves are somewhat more intense (order 20%), as one could expect [*Plougonven et al.*, 2010; *Zhang et al.*, 2013].

References

Alexander, M., and C. Barnet (2007), Using satellite observations to constrain parameterizations of gravity wave effects for global models, *J. Atmos. Sci.*, *64*, 1652–1665.

Alexander, M., et al. (2008), Global estimates of gravity wave momentum flux from High Resolution Dynamics Limb Sounder Observations, *J. Geophys. Res.*, *113*, D15S18, doi:10.1029/2007JD008807.

Alexander, M., et al. (2010), Recent developments in gravity-wave effects in climate models and the global distribution of gravity-wave momentum flux from observations and models, *Q. J. R. Meteorol. Soc.*, *136*, 1103–1124.

Austin, J., et al. (2003), Uncertainties and assessment of chemistry-climate models of the stratosphere, *Atmos. Chem. Phys.*, *3*, 1–27.

Beres, J., M. Alexander, and J. Holton (2004), A method of specifying the gravity wave spectrum above convection based on latent heating properties and background wind, *J. Atmos. Sci.*, *61*, 324–337.

Beres, J., R. Garcia, B. Boville, and F. Sassi (2005), Implementation of a gravity wave source spectrum parameterization dependent on the properties of convection in the Whole Atmosphere Community Climate Model (WACCM), *J. Geophys. Res.*, *110*, D10108, doi:10.1029/2004JD005504.

Boccara, G., A. Hertzog, R. Vincent, and F. Vial (2008), Estimation of gravity-wave momentum fluxes and phase speeds from long-duration stratospheric balloon flights. 1. Theory and simulations, *J. Atmos. Sci.*, *65*, 3042–3055.

Bühler, O., and M. McIntyre (2005), Wave capture and wave-vortex duality, *J. Fluid Mech.*, *534*, 67–95.

Butchart, N., et al. (2010), Chemistry-climate model simulations of twenty-first century stratospheric climate and circulation changes, *J. Clim.*, *23*, 5349–5374.

Chagnon, J., and S. Gray (2008), Analysis of convectively-generated gravity waves in mesoscale model simulations and wind profiler observations, *Q. J. R. Meteorol. Soc.*, *124*, 663–676.

Charron, M., and E. Manzini (2002), Gravity waves from fronts: Parameterization and middle atmosphere response in a general circulation model, *J. Atmos. Sci.*, *59*, 923–941.

Cunningham, P., and D. Keyser (2000), Analytical and numerical modelling of jet streaks: Barotropic dynamics, *Q. J. R. Meteorol. Soc.*, *126*, 3187–3217.

Eckermann, S., and R. Vincent (1993), VHF radar observations of gravity-wave production by cold fronts over Southern Australia, *J. Atmos. Sci.*, *50*, 785–806.

Ern, M., P. Preusse, J. Gille, C. Heppelwhite, M. Mlynczak, J. Russell III, and M. Riese (2011), Implications for atmospheric dynamics derived from global observations of gravity wave momentum flux in stratosphere and mesosphere, *J. Geophys. Res.*, *116*, D19107, doi:10.1029/2011JD015821.

Fritts, D., and M. Alexander (2003), Gravity wave dynamics and effects in the middle atmosphere, *Rev. Geophys.*, *41*(1), 1003, doi:10.1029/2001RG000106.

Fritts, D., and G. Nastrom (1992), Sources of mesoscale variability of gravity waves. Part II: Frontal, convective, and jet stream excitation, *J. Atmos. Sci.*, *49*(2), 111–127.

Geller, M., et al. (2013), A comparison between gravity wave momentum fluxes in observations and climate models, *J. Clim.*, *26*, 6383–6405, doi:10.1175/JCLI-D-12-00545.1.

Gille, J., et al. (2008), High resolution dynamics limb sounder: Experiment overview, recovery and validation of initial temperature data, *J. Geophys. Res.*, *113*, D16S43, doi:10.1029/2007JD008824.

Guest, F., M. Reeder, C. Marks, and D. Karoly (2000), Inertia-gravity waves observed in the lower stratosphere over Macquarie Island, *J. Atmos. Sci.*, *57*, 737–752.

Hertzog, A., and F. Vial (2001), A study of the dynamics of the equatorial lower stratosphere by use of ultra-long-duration balloons: 2. Gravity waves, *J. Geophys. Res.*, *106*, 22,745–22,761.

Hertzog, A., et al. (2007), Stratéole/Vorcore—Long duration, superpressure balloons to study the antarctic stratosphere during the 2005 winter, *J. Atmos. Oceanic Technol.*, *24*, 2048–2061.

Hertzog, A., G. Boccara, R. Vincent, F. Vial, and P. Coquerez (2008), Estimation of gravity-wave momentum fluxes and phase speeds from long-duration stratospheric balloon flights. 2. Results from the Vorcore campaign in Antarctica, *J. Atmos. Sci.*, *65*, 3056–3070.

Hertzog, A., M. Alexander, and R. Plougonven (2012), On the probability density functions of gravity waves momentum flux in the stratosphere, *J. Atmos. Sci.*, *69*, 3433–3448.

Hoskins, B., M. McIntyre, and A. Robertson (1985), On the use and significance of isentropic potential vorticity maps, *Q. J. R. Meteorol. Soc.*, *111*(470), 877–946.

Hoskins, B. J. (1982), The mathematical theory of frontogenesis, *Annu. Rev. Fluid Mech.*, *14*, 131–151.

Hoskins, B. J., and F. P. Bretherton (1972), Atmospheric frontogenesis models: Mathematical formulation and solution, *J. Atmos. Sci.*, *29*, 11–37.

Jewtoukoff, V., R. Plougonven, and A. Hertzog (2013), Gravity waves generated by deep tropical convection: Estimates from balloon observations and mesoscale simulations, *J. Geophys. Res. Atmos.*, *118*, 9690–9707, doi:10.1002/jgrd.50781.

Kim, S.-Y., and H.-Y. Chun (2010), Stratospheric gravity waves generated by typhoon Saomai (2006): Numerical modeling in a moving frame following the typhoon, *J. Atmos. Sci.*, *67*(11), 3617–3636.

Kim, Y.-J., S. Eckermann, and H.-Y. Chun (2003), An overview of the past, present and future of gravity-wave drag parametrization for numerical climate and weather prediction models, *Atmos. Ocean*, *41*, 65–98.

Kirshbaum, D., and D. Durran (2003), Factors governing cellular convection in orographic precipitation, *J. Atmos. Sci.*, *61*, 682–698.

Lambaerts, J., G. Lapeyre, and V. Zeitlin (2012), Moist vs dry baroclinic instability in a simplified two-layer atmospheric model with condensation and latent heat release, *J. Atmos. Sci.*, *69*, 1405–1426.

Lane, T., and J. Knievel (2005), Some effects of model resolution on simulated gravity waves generated by deep, mesoscale convection, *J. Atmos. Sci.*, *62*, 3408–3419.

Lott, F., R. Plougonven, and J. Vanneste (2010), Gravity waves generated by sheared potential vorticity anomalies, *J. Atmos. Sci.*, *67*, 157–170, doi:10.1175/2009JAS3134.1.

Lott, F., R. Plougonven, and J. Vanneste (2012), Gravity waves generated by sheared three-dimensional potential vorticity anomalies, *J. Atmos. Sci.*, *69*, 2134–2151.

Mirzaei, M., C. Zuelicke, A. Moheballojeh, F. Ahmadi-Givi, and R. Plougonven (2014), Structure, energy and parameterization of inertia-gravity waves in dry and moist simulations of a baroclinic wave life cycle, *J. Atmos. Sci.*, *71*, 2390–2414.

O'Sullivan, D., and T. Dunkerton (1995), Generation of inertia-gravity waves in a simulated life cycle of baroclinic instability, *J. Atmos. Sci.*, *52*(21), 3695–3716.

Pavelin, E., J. Whiteway, and G. Vaughan (2001), Observation of gravity wave generation and breaking in the lowermost stratosphere, *J. Geophys. Res.*, *106*(D6), 5173–5179.

Plougonven, R., and C. Snyder (2005), Gravity waves excited by jets: Propagation versus generation, *Geophys. Res. Lett.*, *32*, L18892, doi:10.1029/2005GL023730.

Plougonven, R., and C. Snyder (2007), Inertia-gravity waves spontaneously generated by jets and fronts. Part I: Different baroclinic life cycles, *J. Atmos. Sci.*, *64*, 2502–2520.

Plougonven, R., and F. Zhang (2014), Internal gravity waves from atmospheric jets and fronts, *Rev. Geophys.*, *52*, 33–76, doi:10.1002/2012RG000419.

Plougonven, R., H. Teitelbaum, and V. Zeitlin (2003), Inertia-gravity wave generation by the tropospheric mid-latitude jet as given by the fastex radio soundings, *J. Geophys. Res.*, *108*(D21), 4686, doi:10.1029/2003JD003535.

Plougonven, R., D. Muraki, and C. Snyder (2005), A baroclinic instability that couples balanced motions and gravity waves, *J. Atmos. Sci.*, *62*, 1545–1559.

Plougonven, R., A. Arsac, A. Hertzog, L. Guez, and F. Vial (2010), Sensitivity study for mesoscale simulations of gravity waves above Antarctica during Vorcore, *Q. J. R. Meteorol. Soc.*, *136*(650), 1371–1377.

Plougonven, R., A. Hertzog, and L. Guez (2013), Gravity waves over Antarctica and the Southern Ocean: Consistent momentum fluxes in mesoscale simulations and stratospheric balloon observations, *Q. J. R. Meteorol. Soc.*, *139*, 101–118.

Preusse, P., S. Schroeder, L. Hoffmann, M. Ern, F. Friedl-Vallon, J. Ungermann, H. Oelhaf, H. Fischer, and M. Riese (2009), New perspectives on gravity wave remote sensing by spaceborne infrared limb imaging, *Atmos. Meas. Tech.*, *2*, 299–311.

Preusse, P., M. Ern, P. Bechtold, S. Eckermann, S. Kalisch, Q. Trinh, and M. Riese (2014), Characteristics of gravity waves resolved by ECMWF, *Atmos. Chem. Phys.*, *14*, 10,483–10,508, doi:10.5194/acp-14-10483-2014.

Queney, P. (1948), The problem of air flow over mountains: A summary of theoretical studies, *Bull. Am. Meteorol. Soc.*, *29*, 16–26.

Rabier, F., et al. (2010), The Concordiasi project in Antarctica, *Bull. Am. Meteorol. Soc.*, *91*(1), 69–86.

Ralph, F., P. Neiman, and T. Keller (1999), Deep-tropospheric gravity waves created by leeside cold fronts, *J. Atmos. Sci.*, *56*, 2986–3009.

Reznik, G., V. Zeitlin, and M. B. Jelloul (2001), Nonlinear theory of geostrophic adjustment. Part 1. Rotating shallow-water model, *J. Fluid Mech.*, *445*, 93–120.

Richter, J., F. Sassi, and R. Garcia (2010), Toward a physically based gravity wave source parameterization in a general circulation model, *J. Atmos. Sci.*, *67*, 136–156, doi:10.1175/2009JAS3112.1.

Rind, D., R. Suozzo, N. Balachandran, A. Lacis, and G. Russell (1988), The GISS global climate-middle atmosphere model. Part I: model structure and climatology, *J. Atmos. Sci.*, *45*(3), 329–370.

Sato, K., and M. Yoshiki (2008), Gravity wave generation around the polar vortex in the stratosphere revealed by 3-hourly radiosonde observations at Syowa Station, *J. Atmos. Sci.*, *65*, 3719–3735.

Skamarock, W., J. Klemp, J. Dudhia, D. Gill, D. Barker, M. Duda, X.-Y. Huang, W. Wang, and J. G. Powers (2008), A description of the Advanced Research WRF version 3, *NCAR Tech. Note (NCAR/TN-475+STR)*, Natl. Cent. for Atmos. Res., Boulder, Colo.

Snyder, C., D. Muraki, R. Plougonven, and F. Zhang (2007), Inertia-gravity waves generated within a dipole vortex, *J. Atmos. Sci.*, *64*, 4417–4431.

Snyder, C., R. Plougonven, and D. Muraki (2009), Forced linear inertia-gravity waves on a basic-state dipole vortex, *J. Atmos. Sci.*, *66*(11), 3464–3478.

Song, I.-S., and H.-Y. Chun (2005), Momentum flux spectrum of convectively forced internal gravity waves and its application to gravity wave drag parameterization. Part I: Theory, *J. Atmos. Sci.*, *62*, 107–124.

Stephan, C., and M. Alexander (2014), Summer season squall line simulations: Sensitivity of gravity waves to physics parameterization and implication for their parameterization in global climate models, *J. Atmos. Sci.*, *71*, 3376–3391, doi:10.1175/JAS-D-13-0380.1.

Thomas, L., R. Worthington, and A. McDonald (1999), Inertia-gravity waves in the troposphere and lower stratosphere associated with a jet stream exit region, *Ann. Geophys.*, *17*, 115–121.

Uccelini, L., and S. Koch (1987), The synoptic setting and possible energy sources for mesoscale wave disturbances, *Mon. Weather Rev.*, *115*, 721–729.

Vallis, G. (2006), *Atmospheric and Oceanic Fluid Dynamics*, 745 pp., Cambridge Univ. Press, Cambridge, U. K.

Vanneste, J. (2004), Inertia-gravity wave generation by balanced motion: Revisiting the Lorenz-Krishnamurty model, *J. Atmos. Sci.*, *61*, 224–234.

Vanneste, J. (2008), Exponential smallness of inertia-gravity-wave generation at small Rossby number, *J. Atmos. Sci.*, *65*, 1622–1637.

Vanneste, J. (2013), Balance and spontaneous wave generation in geophysical flows, *Annu. Rev. Fluid Mech.*, *45*, 147–172.

Vincent, R., A. Hertzog, G. Boccara, and F. Vial (2007), Quasi-Lagrangian superpressure balloon measurements of gravity-wave momentum fluxes in the polar stratosphere of both hemispheres, *Geophys. Res. Lett.*, *34*, L19804, doi:10.1029/2007GL031072.

Viudez, A. (2007), The origin of the stationary frontal wave packet spontaneously generated in rotating stratified vortex dipoles, *J. Fluid Mech.*, *593*, 359–383.

Viudez, A. (2008), The stationary frontal wave packet spontaneously generated in mesoscale dipoles, *J. Phys. Oceanogr.*, *38*, 243–256.

Waite, M. L., and C. Snyder (2012), Mesoscale energy spectra of moist baroclinic waves, *J. Atmos. Sci.*, *70*(4), 1242–1256.

Wang, S., and F. Zhang (2007), Sensitivity of mesoscale gravity waves to the baroclinicity of jet-front systems, *Mon. Weather Rev.*, *135*, 670–688.

Wang, S., and F. Zhang (2010), Source of gravity waves within a vortex-dipole jet revealed by a linear model, *J. Atmos. Sci.*, *67*, 1438–1455.

Wang, S., F. Zhang, and C. Snyder (2009), Generation and propagation of inertia-gravity waves from vortex dipoles and jets, *J. Atmos. Sci.*, *66*, 1294–1314.

Wang, S., F. Zhang, and C. Epifanio (2010), Forced gravity wave response near the jet exit region in a linear model, *Q. J. R. Meteorol. Soc.*, *136*, 1773–1787.

Wang, W., et al. (2012), *Advanced Research WRF: Version 3 Modeling System Users' Guide*, p. 384, Natl. Cent. for Atmos. Res., Boulder, Colo.

Wei, J., and F. Zhang (2014), Mesoscale gravity waves in moist baroclinic jet-front systems, *J. Atmos. Sci.*, *71*, 929–952, doi:10.1175/JAS-D-13-0171.1.

Yamanaka, M., S. Fukao, H. Matsumoto, T. Sato, T. Tsuda, and S. Kato (1989), Internal gravity wave selection in the upper troposphere and lower stratosphere observed by the MU radar: Preliminary results, *Pure Appl. Geophys.*, *130*, 481–495.

Yan, X., N. Arnold, and J. Remedios (2010), Global observations of gravity waves from High Resolution Dynamics Limb Sounder temperature measurements: A yearlong record of temperature amplitude and vertical wavelength, *J. Geophys. Res.*, *115*, D10113, doi:10.1029/2008JD011511.

Zeitlin, V. (2008), Decoupling of balanced and unbalanced motions and inertia-gravity wave emission: Small versus large rossby numbers, *J. Atmos. Sci.*, *65*(11), 3528–3542.

Zhang, F. (2004), Generation of mesoscale gravity waves in upper-tropospheric jet-front systems, *J. Atmos. Sci.*, *61*(4), 440–457.

Zhang, F., S. Koch, C. Davis, and M. Kaplan (2001), Wavelet analysis and the governing dynamics of a large amplitude mesoscale gravity wave event along the East Coast of the United States, *Q. J. R. Meteorol. Soc.*, *127*, 2209–2245.

Zhang, F., M. Zhang, J. Wei, and S. Wang (2013), Month-long simulations of gravity waves over North America and North Atlantic in comparison with satellite observations, *Acta Meteorol. Sin.*, *27*, 446–454, doi:10.1007/s13351-013-0301-x.